Dual-mode Imaging System for Early Detection and Monitoring of Ocular Surface Diseases

Yuxing Li, Pak Wing Chiu, Vincent Tam, *Senior Member, IEEE,* Allie Lee,
and Edmund Y. Lam, *Fellow, IEEE*

***Abstract*—The global prevalence of ocular surface diseases (OSDs), such as dry eyes, conjunctivitis, and subconjunctival hemorrhage (SCH), is steadily increasing due to factors such as aging populations, environmental influences, and lifestyle changes. These diseases affect millions of individuals worldwide, emphasizing the importance of early diagnosis and continuous monitoring for effective treatment. Therefore, we present a deep learning-enhanced imaging system for the automated, objective, and reliable assessment of these three representative OSDs. Our comprehensive pipeline incorporates processing techniques derived from dual-mode infrared (IR) and visible (RGB) images. It employs a multi-stage deep learning model to enable accurate and consistent measurement of OSDs. This proposed method has achieved a 98.7% accuracy with an F1 score of 0.980 in class classification and a 96.2% accuracy with an F1 score of 0.956 in SCH region identification. Furthermore, our system aims to facilitate early diagnosis of meibomian gland dysfunction (MGD), a primary factor causing dry eyes, by quantitatively analyzing the meibomian gland (MG) area ratio and detecting gland morphological irregularities with an accuracy of 88.1% and an F1 score of 0.781. To enhance convenience and timely OSD management, we are integrating a portable IR camera for obtaining meibography during home inspections. Our system demonstrates notable improvements in expanding dual-mode image-based diagnosis for broader applicability, effectively enhancing patient care efficiency. With its automation, accuracy, and compact design, this system is well-suited for early detection and ongoing assessment of OSDs, contributing to improved eye healthcare in an accessible and comprehensible manner.**

***Index Terms*—ocular surface diseases, deep learning, precision eye healthcare, home inspection, early identification, monitoring system**

I. INTRODUCTION

THE ocular surface, a critical and essential component of vision, is particularly susceptible to desiccation, injury, and pathogens due to its direct exposure to external factors [1]. Ocular surface diseases (OSDs) encompass a diverse array of conditions affecting the delicate tissues of the eye surface, such as the cornea, conjunctiva, and eyelids [2]. The worldwide prevalence of OSD, diagnosed based on symptoms, varies between 7% to 52% [3], posing significant challenges to global eye health. OSDs, such as dry eyes, conjunctivitis, and subconjunctival hemorrhage (SCH), can cause discomfort, pain, redness, and vision impairment, affecting an individual's overall eye health and quality of life. These conditions also contribute to psychological distress, often disrupting daily activities. Moreover, OSDs impose a considerable economic burden on society, encompassing both direct costs, such as medical expenses and treatment, and indirect costs, like lost productivity and time spent seeking care [4]. Many OSDs are commonly undiagnosed due to the absence of standardized symptom descriptions and the numerous subtypes of OSD in practice [5]. Therefore, efficient diagnosis and ongoing monitoring of OSDs are essential for preserving visual function, enhancing patient well-being, and alleviating the socioeconomic burden associated with these prevalent eye conditions [6]. However, conventional visual examination techniques may be constrained by the availability of proficient medical experts and variability between observers, potentially resulting in inconsistencies in diagnosis and patient treatment. Moreover, the chronic and progressive nature of many OSDs necessitates long-term monitoring to assess treatment efficacy and disease progression.

Given these challenges, there is a pressing need for a system that can automatically, objectively, and reliably evaluate OSDs. Such systems can overcome the limitations of human variability and expertise, reducing diagnostic discrepancies and enhancing the efficacy of treatments. Moreover, automation in diagnostics can accelerate the assessment process, facilitating prompt interventions and thereby, improving patient care outcomes. This is particularly crucial in remote regions where access to specialized healthcare is limited. The latest progress in assessing ophthalmic diseases through the use of neural networks presents a promising direction toward data-driven automation development [7]. In the field of ophthalmology, deep learning methods have primarily been utilized for the screening and diagnosis of fundus-related conditions, including diabetic retinopathy and glaucoma. The relatively consistent nature of fundus images allows for easier standardization in analysis [8]. However, limited research has been conducted on integrating deep learning for the automatic evaluation of external eye images, especially for multiple external eye diseases and various image types. A primary challenge in researching OSDs lies in the complexity of the images involved, which consist of multiple modalities. Therefore, it is essential to develop an effective method for analyzing these complex images and accurately diagnosing OSDs using advanced deep learning techniques [9]. For instance, machine learning methodologies, such as random forests and multi-layer perceptron, have demonstrated effectiveness in evaluating external eye redness [10]. These approaches have been used to segment the sclera region and grade conjunctival hyperemia. Moreover,

Yuxing Li, Vincent Tam, and Edmund Y. Lam are with the Department of Electrical and Electronic Engineering, The University of Hong Kong, Pokfulam, Hong Kong (e-mail: yuxingli@hku.hk; elam@eee.hku.hk)

Pak Wing Chiu and Allie Lee are with the Department of Ophthalmology, The University of Hong Kong, Pokfulam, Hong Kong

deep learning techniques, particularly convolutional neural networks (CNNs), have been utilized to distinguish between dry eyes and healthy ones according to image [11] or video features [12] features. The continuous improvement in OSD image processing techniques demonstrates the growing focus on automating detection, highlighting the field's progression towards enhanced diagnostic precision.

Multimodal images play a vital role in differentiating various types of OSDs. By incorporating multiple imaging techniques, such as slit-lamp photography and infrared (IR) meibography, a more comprehensive and detailed assessment of the ocular surface can be achieved [13]. The slit-lamp photos with color can reflect ocular redness, a prevalent symptom that manifests as an abnormal reddish hue or increased visibility of blood vessels in the eye. This redness is a distinguishing feature of numerous eye conditions, such as conjunctivitis, SCH, and ocular allergies [14]. Conjunctivitis can be classified into bulbar conjunctivitis and palpebral (or tarsal) conjunctivitis based on the anatomical location of the inflammation within the conjunctiva. This paper focuses on bulbar conjunctivitis, characterized by inflammation of the bulbar conjunctiva, and distinguishes it from SCH, a condition that often causes patient anxiety due to its similar appearance. Recognizing the distinction between these conditions is crucial for proper management and treatment. While SCH typically resolves on its own, bulbar conjunctivitis may require medical intervention, depending on the severity and underlying cause. Accurate diagnosis is essential to avoid mismanagement and alleviate patient concerns regarding the nature of their symptoms. Furthermore, meibography, a non-invasive technique, is essential for assessing the health of the meibomian glands (MGs), crucial in the diagnosis and management of conditions like dry eye syndrome and meibomian gland dysfunction (MGD). MGD is the leading cause of evaporative dry eye, impacting lipid secretion and tear evaporation. It has been reported that 80% to 90% of dry eye patients exhibit signs of MGD [15], [16]. The morphology of MGs, evaluated through meibography, is directly related to the severity of MGD. MG image indexes serve as significant markers for gland health, and a widely used measure for evaluating MGD is the extent of MG atrophy [8], [17], [18]. These diverse imaging modalities provide valuable insights into the structure and function of the cornea, conjunctiva, and MGs, which are critical for understanding the underlying causes and manifestations of OSDs. Furthermore, multimodal imaging allows for the identification of subtle changes and abnormalities that might be missed by a single imaging method [19]. As a result, ophthalmologists can make more accurate diagnoses and develop targeted treatment plans for patients suffering from various OSDs, such as dry eye syndrome, conjunctivitis, SCH, and MGD. Overall, the use of multimodal images significantly enhances the precision and effectiveness of OSD evaluation and management.

Given that many OSDs are chronic in nature, continuous monitoring becomes vital in ensuring appropriate treatment and symptom management. Unfortunately, the majority of available diagnostic tools and monitoring techniques are clinic-based, requiring patients to visit eye care professionals, which may not be feasible for continuous monitoring. It has been reported that only 33.6% of dry eye patients received a follow-up examination within six months, highlighting the challenge of maintaining long-term monitoring in clinical settings [20]. To tackle insufficient home inspection and long-term monitoring, telemedicine presents a promising strategy for diagnosing OSDs, improving access to ophthalmic care, particularly in light of the widespread adoption of smartphones and their combination with relevant portable IR camera devices [21]. To the best of our knowledge, no existing prototype comprehensively addresses multiple types of OSDs. At present, only a few commercially available portable IR meibographers, such as MeiboVue and Ezer Sapphire, are capable of capturing MG images [22]. Although these devices offer high-resolution meibography for diagnostic purposes, they fall short in providing accurate measurement and quantification of MG morphology. Furthermore, these devices lack automated algorithms for the early detection of MG irregularities and are unable to offer patients personalized recommendations based on their specific conditions.

In this work, an extended version of [23], we present an innovative automatic external eye disease monitoring system that offers a comprehensive pipeline, integrating a variety of image processing techniques derived from dual-mode information of IR and visible (RGB) images. Moreover, our system employs a multi-stage deep learning model to accomplish effective and consistent quantification of OSDs. The primary objective of our approach is to facilitate early diagnosis of MGD, a leading cause of dry eyes, by accurately analyzing the MG area and ratio, as well as identifying structural and functional abnormalities of the glands. Additionally, our system strives to enhance the classification and tracking of ocular redness patterns associated with SCH and bulbar conjunctivitis, enabling better identification of these conditions. Our system extends beyond the mere detection of ocular redness to encompass a wide range of OSDs, offering a more comprehensive approach to OSD diagnosis and management compared to prior studies. The inclusion of a portable IR camera in our dual-mode imaging setup allows for easy at-home inspections, promoting more frequent monitoring of OSDs for timely identification and management. By leveraging advanced image processing methods and deep learning models, our monitoring system offers a more accurate and reliable assessment of external eye diseases, which is crucial for the development of targeted treatment plans and improved patient outcomes. Furthermore, this automated system can significantly reduce the workload of ophthalmologists and support clinical decision-making by providing objective and consistent evaluations of ocular surface conditions. Ultimately, our work seeks to make a meaningful contribution to the field of ophthalmology by enhancing patient care and streamlining the diagnosis and management of common OSDs.

II. METHODS

A dual-mode assessment system necessitates various detection and quantification results from multiple stages. Initially, we train deep learning models in tandem style using bimodal ophthalmic images for the precise detection and monitoring

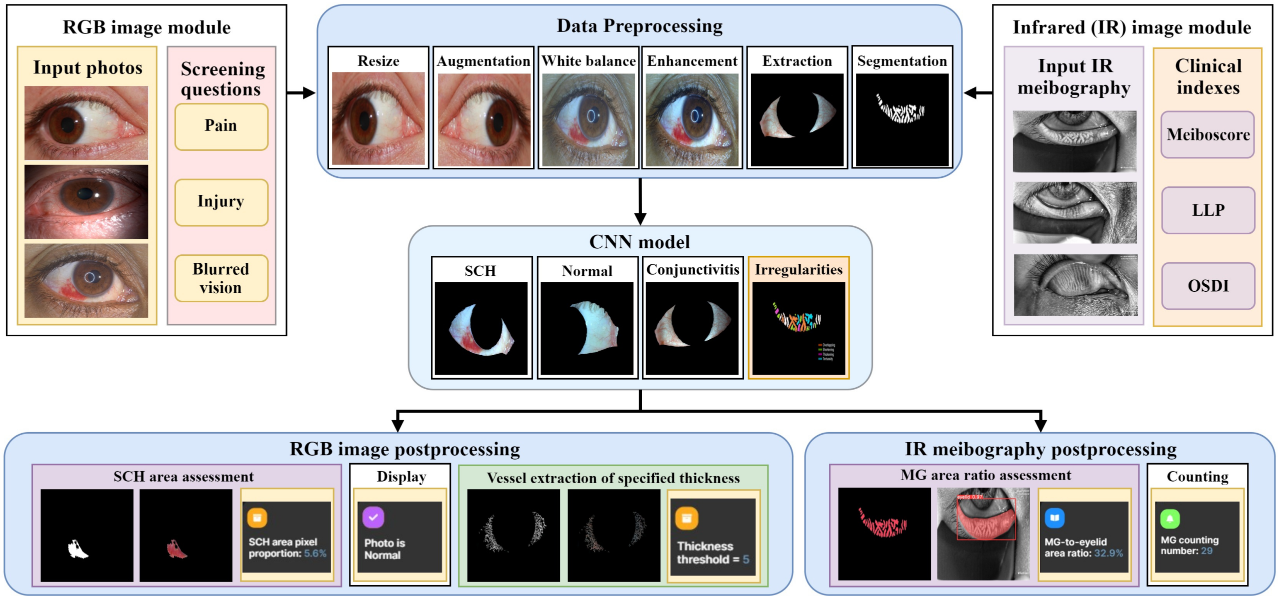

Fig. 1. The dual-mode imaging system pipeline consists of three primary steps: data preprocessing, OSD diagnosis using CNN models, and data postprocessing. The input data is divided into two modules: RGB external ocular images and IR meibography images, which are used for extracting features and performing classification. To enhance the evaluation of OSDs, relevant screening questions or clinical indices are integrated as supplementary references, facilitating a comprehensive assessment of OSDs. OSDI: Ocular surface disease index, LLP: Lipid layer pattern.

of OSDs. Subsequently, we enhance the system with portable imaging devices to improve medical delivery. The algorithm architecture, depicted in Fig. 1, is composed of three primary elements: data preprocessing engines, the multi-stage model, and postprocessing. Two types of ophthalmic images serve as input: RGB scleral images and IR meibography images. In the initial screening of the dataset images, factors such as intensity, contrast, and resolution are considered. The RGB images of the sclera are categorized as normal, SCH, or bulbar conjunctivitis, while the IR meibography images are treated as a separate input. The system employs image preprocessing methods, including resizing and augmentation, white balance adjustment, contrast enhancement, scleral or eyelid area extraction, and MG region segmentation. The processed data is then input into the customized models for classification and diagnosis. Subsequently, specific quantification measurements are performed, and monitoring parameters are provided according to the diagnosis. The efficiency of the suggested framework is assessed by scleral or eyelid segmentation, eye redness classification, SCH area measurement, extraction of vessels with specific thicknesses, MG area segmentation, and MG irregularity identification.

A. Image preprocessing

1) Data acquisition and annotations: Dual-mode ophthalmic images are utilized in this study, which are advantageous for addressing various OSDs and enhancing diagnostic accuracy. All data is anonymized to ensure patient privacy, and Institutional Review Boards (IRB) approvals have been secured to protect human research subjects' rights.

For the visible (RGB) image module, this work employed two distinct datasets. the External Eye Photo (EEP) dataset obtained from the Lo Fong Shiu Po Eye Centre (LFSC) in Hong Kong, and the publicly accessible Sclera Blood Vessels, Periocular, and Iris (SBVPI) dataset [24]. These diverse datasets improve the system's generalization abilities and ensure unbiased performance. The EEP dataset includes 600 external eye images (2576×1934) across three categories (SCH 200, bulbar conjunctivitis 200, and normal 200). The SBVPI dataset encompasses 1840 external eye images (3000×1700) from 55 subjects [25].

For the IR image module, 1200 IR meibography images are gathered from 378 patients in total. 200 images (820×615) were obtained from 58 patients who visited LFSC for dry eye evaluations. During the visits, meibography images of the upper and lower eyelids for both eyes were captured. Furthermore, the publicly available MGD-1K dataset includes 1000 images (1280×640) from 320 patients, with 467 images of upper eyelids and 533 of lower eyelids [26]. The IR MG images are taken using the LipiView interferometer (Johnson & Johnson Inc., USA), a clinical instrument that uses near-infrared illumination for MG imaging.

Annotation efforts for RGB and IR images from LFSC involve manual labeling by a skilled team using the polygon selection tool of ImageJ software (Bethesda, USA) [27]. RGB images are annotated to identify scleral regions, SCH areas, and blood vessels, while IR images are marked to delineate eyelid regions and MG areas. Rigorous revisions ensure the segmentation's accuracy. The analysis of segmented RGB sclera images categorizes them into normal, SCH, and bulbar conjunctivitis groups, including area measurements and vessel analysis. For IR meibography images, the focus is on segmenting MG areas, identifying abnormal MG morphologies, and conducting further assessments of MG area ratios and irregularities.

2) Image resizing, contrast enhancement, and white-balancing adjustment: Both RGB and IR images are resized to 640×640 pixels to ensure uniformity in image dimensions and computational cost during training. Given the inherent variations in quality among input images, standardization is crucial for enhancing the visibility and evaluation performance. For low-contrast images with intricate details, histogram equalization is applied to enhance the global contrast of images, especially when the valuable information in the image is represented by close contrast values [28]. This process involves spreading out the most frequent intensity values and adjusting the intensities on the histogram to achieve better distribution and higher contrast.

Images captured under diverse lighting conditions for various patients typically exhibit variations in brightness and color temperature, which can potentially impact the assessment and diagnosis of OSDs. The classification and segmentation processes are particularly sensitive to the color temperature of RGB images. To address this challenge, we employed automatic white balance algorithms designed to estimate the color temperature of the light source and subsequently harmonize the colors within the images [29]. The application of the gray world assumption ensures that disparate images maintain consistent color temperatures. Furthermore, image augmentation is employed to expand the dataset and enhance the training of the network. By employing diverse transformations, including scaling, rotation, and flipping, we enhance the variety and total quantity of the dataset. This enriched dataset contributes to the model's improved generalization and reduces overfitting.

3) Segmentation of the scleral or eyelid area: Processing external eye images or meibography images can encounter challenges due to skin and eyelash interference. Therefore, it is essential to accurately segment the scleral region of RGB eye images or eyelid region of IR meibography before proceeding with subsequent classification steps. CNNs have demonstrated superior efficacy compared to conventional methods in tasks involving semantic image segmentation. Specifically, the U-Net architecture is widely utilized in biomedical image segmentation applications [30]. In our study, the U-Net architecture is employed for scleral or eyelid region segmentation, and to avoid ambiguity, the network is referred to as SU-Net. The training involves the utilization of external eye pictures and their respective scleral region annotations for RGB images, as well as meibography images and associated labeling of the eyelid area for IR images. The binary cross-entropy loss is employed as the loss function, which is mathematically expressed as

$$\text{Binary Loss} = -(y \cdot \log(p) + (1-y) \cdot \log(1-p)) \qquad (1)$$

where y is the true class label (0 or 1) and p represents the predicted probability of belonging to the positive class (class 1).

The ADAM optimizer is applied as the adaptive learning rate during network training, beginning with an initial learning rate. While performing the inference, the SU-Net generates a binary mask for the scleral or eyelid area. This mask is then used to separate the scleral or eyelid region from the external eye photographs or meibography images, ultimately yielding the scleral or eyelid image.

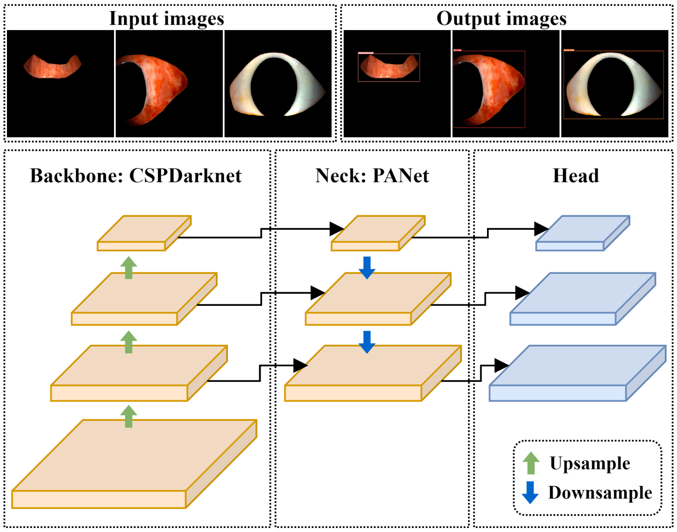

Fig. 2. YOLOv5 architecture for RGB image classification, featuring a CSPDarknet backbone for feature extraction, a PANet neck for feature fusion, and a head to output class (Normal, SCH, or bulbar conjunctivitis), score, and location.

B. Multi-satge deep learning model

The application of multi-stage deep learning in ophthalmic image classification and segmentation offers a promising approach to enhancing the diagnosis and monitoring of various eye diseases and conditions. By breaking down the overall task into smaller subtasks, each deep learning model can focus on a specific aspect of the image analysis process, such as feature extraction, classification, or segmentation. This modular approach not only improves the accuracy of the results but also facilitates scalability, enabling the processing of large-scale ophthalmic image datasets. Moreover, the modularity of multi-stage deep learning system allows for independent training, optimization, and updating of each model, simplifying maintenance and customization. Lastly, decomposing the problem into smaller, more interpretable subtasks can provide better insights into the contributions of each stage to the final classification or segmentation outcome.

1) Classification of SCH and bulbar conjunctivitis using RGB external eye images: Among various CNN models, YOLOv5 is distinguished by its lightweight nature, allowing it to operate on mobile electronic devices equipped with only a CPU [31]. As a one-stage object detection method, YOLO offers a fast end-to-end approach to identifying objects. Its neural network architecture predicts a set of bounding boxes and their associated class probabilities. The YOLOv5 architecture integrates multiple scales and resolution strategies, enhancing its adaptability to a wide range of image sizes and scales. Its versatility and performance make YOLOv5 a valuable tool for tasks such as lesion detection or anatomical structure localization in medical images, where rapid and precise object detection is essential [32]. In order to optimize system efficiency, we primarily utilize YOLOv5 for image classification.

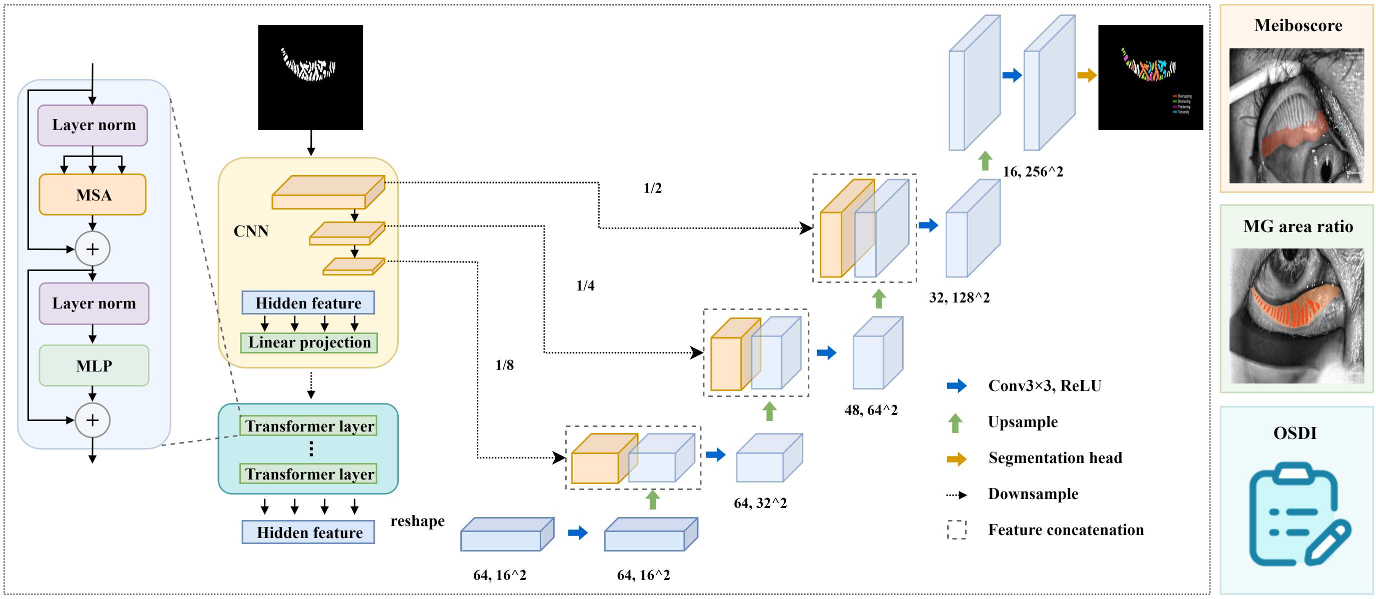

Fig. 3. An overview of the customized TransUNet architecture with an illustration of the transformer layer. MSA: Multihead Self-Attention, MLP: Multi-Layer Perceptron.

For RGB external eye images, YOLOv5 is employed to classify SCH, bulbar conjunctivitis, and normal cases. Differentiating between similar eye redness found in SCH and bulbar conjunctivitis can be challenging in certain situations. Accurate assessment and diagnosis are crucial, as distinct approaches are required for these two different types of eye redness. The YOLOv5 architecture comprises dataset images, backbone, neck, head, and detection output components, as depicted in Fig. 2 [33].

The data processing begins with CSPDarknet, which extracts features from the input. These features are then integrated through the Path Aggregation Network (PANet) for fusion, culminating in the head layer, which delivers the detection outcomes, including class, score, and bounding box details. The backbone, or core of the YOLOv5 network, focuses on extracting relevant information from the input images. CSPDarknet technology within the backbone addresses the issue of repetitive gradient information, optimizing the blend of gradient variation and feature maps. This reduces the model's size while maintaining low parameter count and FLOPS, thereby enhancing inference accuracy and efficiency [34]. Furthermore, YOLOv5 utilizes the PANet as its neck to strengthen information flow [35]. PANet introduces a new Feature Pyramid Network (FPN) structure and an enhanced bottom-up path to improve low-level feature distribution. It also employs adaptive feature pooling to facilitate the direct transmission of useful information to subsequent layers, thus improving object localization precision. The incorporation of a preprocessing engine further boosts the model's efficiency and accuracy.

2) Identification of eye redness or MG morphology: Transformers are renowned for their robust self-attention mechanisms, which enhance the ability to capture global contextual information. The transformer mechanism proves effective in understanding relationships between distant pixels in images, and this capability is particularly beneficial in medical image segmentation tasks. TransUNet combines the strengths of Transformers and U-Net, establishing it as a powerful choice for medical image segmentation and a current state-of-the-art method [36]. While U-Net excels at local feature extraction, TransUNet extends this capability by incorporating a more global perspective. This advantage makes TransUNet well-suited for tasks where capturing both fine-grained details and broader contextual information is essential [37], [38]. The training process employs a mixed loss function of Dice Loss and Cross-Entropy Loss. The Dice Loss function is mathematically expressed as

$$\text{Dice Loss} = 1 - \frac{2 \cdot |A \cap B|}{|A| + |B|} \tag{2}$$

where A represents the ground truth segmentation and B is the predicted segmentation.

In this study, we adapted the TransUNet model to automatically and precisely segment the reddish area in classified SCH images and predict the vessel map in bulbar conjunctivitis images. Additionally, the model is trained to segment MG regions in meibography images. Assessing MGs remains crucial for a comprehensive understanding of dry eye pathophysiology, with MG dropout being a key index for evaluating MGD. To further refine the identification of abnormal MGs, which serve as early indicators of potential dropouts, the MG irregularities are categorized into overlapping, shortening, thickening, and tortuosity. As depicted in Fig. 3, the architecture of TransUNet features a CNN-Transformer hybrid as the encoder, paired with a conventional cascaded upsampler as the decoder. Modifications to the original TransUNet design include setting the number of feature channels for encoding levels at 16, 32, 48, and 64, respectively. Both the downsampling and upsampling stages have been simplified to a single convolutional layer stack. Additionally, the architecture includes a single transformer block and attention head. The transformer's Multilayer Perceptrons are equipped with a Gaussian Error Linear Unit (GELU) [39], whereas a Rectified Linear Unit (ReLU) follows the convolutional layers, complemented by a sigmoid output activation function and batch normalization. Downsampling and upsampling processes are executed through max-pooling and bilinear interpolation, respectively. To optimize hyperparameters such as learning rate, batch size, and the use of augmentations, a manual grid search is conducted. This model is initialized with pre-trained weights from the Vision Transformer (ViT) and subsequently fine-tuned for the specific task of identifying abnormal MGs. Additionally, we incorporated clinical metrics such as Meiboscore, MG area ratio, and Ocular Surface Disease Index (OSDI) to enhance the model's diagnostic utility.

3) Model training: Our study introduces a multi-stage deep learning model combining YOLOv5 for object classification and TransUNet for precise segmentation of the classified regions. Initially, YOLOv5 efficiently categorizes the input data, which is then refined through the precise segmentation capabilities of TransUNet. This sequential methodology enhances the model's ability to deliver more accurate and detailed predictions by leveraging the strengths of both classification and segmentation processes. The integration of YOLOv5 and TransUNet provides a comprehensive framework for analyzing input data, where YOLOv5's rapid object classification is complemented by TransUNet's detailed segmentation, optimizing the overall performance of the model. We employ a stage-wise training strategy, allowing each component to be independently trained while ensuring that the output from one stage aligns with the input requirements of the next, both in format and semantic content.

For algorithm development, the dataset is partitioned into two subsets: a training set for model training and a validation set for hyperparameter tuning (e.g., network architectures, learning rate, etc.). The evaluation set, distinct from the development dataset, is used to assess the model's performance, selecting the best-performing model based on validation results. The development and training of deep learning models are executed using the PyTorch framework, with computational support from an Nvidia RTX 4090 graphics card. Data visualization, including scatter diagrams and line charts, is conducted using GraphPad Prism software (GraphPad Inc, USA).

4) Performance Evaluation: Stage-wise evaluation is applied to evaluate the performance of each stage independently to identify and address bottlenecks or underperformance issues. To assess the effectiveness of the proposed model, various performance metrics have been computed in this study. Accuracy, Precision, Recall, F1 score, and the AUC (Area Under the Curve) of the ROC (Receiver Operating Characteristics) curve have been determined to provide a comprehensive evaluation.

$$Accuracy = \frac{TP + TN}{TP + TN + FP + FN} \tag{3}$$

$$IOU = \frac{TP}{FP + FN + TP} \tag{4}$$

$$Precision = \frac{TP}{TP + FP} \tag{5}$$

$$Recall = \frac{TP}{TP + FN} \tag{6}$$

$$Specificity = \frac{TN}{TN + FP} \tag{7}$$

$$F1score = \frac{2 \times Precision \times Recall}{Precision + Recall} \tag{8}$$

The mathematical formulas in Equations (3)–(8) outline the calculations for accuracy, Intersection over Union (IOU), Precision, Recall, Specificity, and F1 score, involving true positive (*TP*), false positive (*FP*), true negative (*TN*), and false negative (*FN*). Specifically, *TP* refers to the count of correct classifications of the positive class, while *TN* represents the count of correct classifications of the negative class. *FP* is the count of incorrect classifications of the positive class, and *FN* indicates the count of incorrect classifications of the negative class.

Precision measures the proportion of true positive predictions relative to all positive predictions made by the model, highlighting its ability to identify diseased cases with minimal false positives. Recall, or sensitivity, assesses the model's effectiveness in detecting actual diseased cases within the dataset, crucial for early diagnosis and prevention. The F1-score, a harmonic mean of precision and recall, provides a balanced metric of model performance, particularly useful in imbalanced datasets or when the impact of false positives and negatives varies. It ranges from 0 to 1, with higher values indicating better performance. Furthermore, we employed an AUC-ROC graph, a widely utilized visualization tool in the medical domain. The AUC quantifies the discriminative ability of the model, reflecting its capacity to distinguish between positive and negative instances. The ROC curve plots the true positive rate against the false positive rate, illustrating the trade-off between sensitivity and specificity [40]. The use of AUC-ROC aids in evaluating the model's overall performance and its suitability for medical data analysis.

To assess the reliability of a computer-based approach, one-way Analysis of Variance (ANOVA) statistical analysis is employed to compare the means across several groups [10]. One-way ANOVA is employed when there are more than two groups to assess whether there are significant differences in the means of a continuous variable. To evaluate a deep learning model, k-fold cross-validation is commonly utilized. In this research, we applied k=5. Both the RGB and IR image datasets are independently divided. For each of these two modules, the images are randomly split into five sub-groups. In every fold of the validation process, four groups are selected as the training dataset, while one group serves as the validation dataset for training the model [41]. Furthermore, to validate the robustness and generalizability of our model, external validation is performed using an independent Kaggle dataset.

This external dataset, not used during the model training and internal validation phases, is obtained from different clinical settings and includes a diverse range of subjects. By evaluating the model's performance using the external data source, we ensure its applicability across various clinical environments.

C. Data Postprocessing

1) SCH area measurement and vessel extraction of specific thicknesses: In our comprehensive eye care approach, assessment follows classification. For input images identified as containing SCH, we calculate the SCH region's area using a custom Python script. The total pixel number within the SCH region and scleral area are counted. Subsequently, the proportion of SCH-area pixels in the scleral region is determined to monitor daily changes. In the case of bulbar conjunctivitis classification, we extract vessels of specified thickness for precise measurements [42]. A specialized script, utilizing predicted vessel maps, generates a binary image containing vessels of designated thickness. This process involves employing various image-processing techniques, including morphological operations and filtering [43].

For input images identified as having bulbar conjunctivitis, we implement a sequence of procedures to isolate vessels of designated thicknesses, involving the input of the original scleral image and its corresponding vessel probability map. The outcome is a binary image that specifically includes vessels of the designated thicknesses. To achieve this, we utilize a multi-scale vessel enhancement technique relying on the Frangi filter [44]. This method is adept at enhancing and distinguishing closely positioned elongated structures across multiple scales [45].

2) MG area ratio and morphological irregularity assessment: The MG area ratio is utilized as an indicator to evaluate the health and functionality of MGs within the eyelids. This metric quantifies the proportion of the visible MG area relative to the total eyelid area, with a higher MG area ratio signifying healthier MGs, indicative of optimal lipid secretion and ocular surface protection. Conversely, a reduced MG area ratio may suggest the presence of MGD. The analysis includes a comparison between the computed MG area ratio and ground truth value to ascertain accuracy.

Following the segmentation of MGs, additional morphological metrics are assessed. This involves the computation of various morphometric parameters, such as the number of glands, along with their length, width, and area ratio for each individually segmented gland. Meibography images are classified into four groups based on meiboscore (range, 0-3), and the MG irregularity ratios in each group are analyzed. In this study, we employed a standardized MG atrophy grading scale to categorize percent atrophy according to its severity. We used a previously published clinical grading system, known as the meiboscore [46], [47], as illustrated in Table I.

TABLE I
CRITERIA FOR CONVERTING PERCENT MG ATROPHY TO MEIBOSCORE [46]

MG Atrophy, %	Meiboscore
0	0
0-33	1
33-66	2
over 66	3

We categorize MG irregularities into four specific types: overlapping, shortening, thickening, and tortuosity. To analyze these irregularities, meibography images are divided into four distinct groups according to the meiboscore, ranging from 0 to 3. By evaluating the ratios of MG irregularities within each group, we can attain a more comprehensive understanding of glandular abnormalities. This approach contributes to the early detection and efficient management of MGD and associated OSDs. In this process, clinical indices are integrated into the evaluation to examine the relationship.

D. Imaging Technique Integration

To capture dual-mode images, distinct imaging methodologies are essential for acquiring both RGB and IR photographs. RGB images can be easily obtained using RGB cameras or smartphones by patients, while IR imaging necessitates additional specialized equipment for meibography acquisition. Integrating a portable IR camera facilitates at-home meibography inspections, significantly improving access and convenience for patients, particularly those facing mobility challenges or limited healthcare access. This advancement allows for the comfort of home-based inspections, promoting early detection and regular monitoring of MGD, a task less achievable with conventional clinical imaging tools.

To facilitate IR image acquisition, a handheld device featuring a specialized 2.0-megapixel IR USB camera (Zhongweiaoke Inc, CN) is integrated into the system (Fig. 16). The image size is 1920×1080 pixels, which meets diagnostic requirements. The camera incorporates a 90-degree angle-of-view (AOV) module, which prevents image distortion. For improved image capturing, the device is furnished with six LED lights with a wavelength of $850\,\mathrm{nm}$ and a narrow band filter, which is also the typical wavelength for clinical-based meibography imaging machines. The encapsulated meibography imager has a size of $3.5\,\mathrm{cm}\times 3.5\,\mathrm{cm}\times 1\,\mathrm{cm}$ as shown in Fig. 17. This compact and portable meibography technology has an approximate working distance of $5\,\mathrm{cm}$, making it suitable for use in both clinical environments and home inspections in capturing detailed images of the MG structure.

The handheld device is specifically designed for seamless integration with widely used operating systems such as Windows OS and Android OS, eliminating the need for additional setup or drivers. This compatibility further includes smartphones, enabling easy pairing and improving the device's portability and user-friendly characteristics. Through the combination of advanced imaging capabilities and a compact, user-friendly design, this meibography technology presents a practical solution for eye care professionals aiming to efficiently assess MG health and diagnose associated OSDs [48].

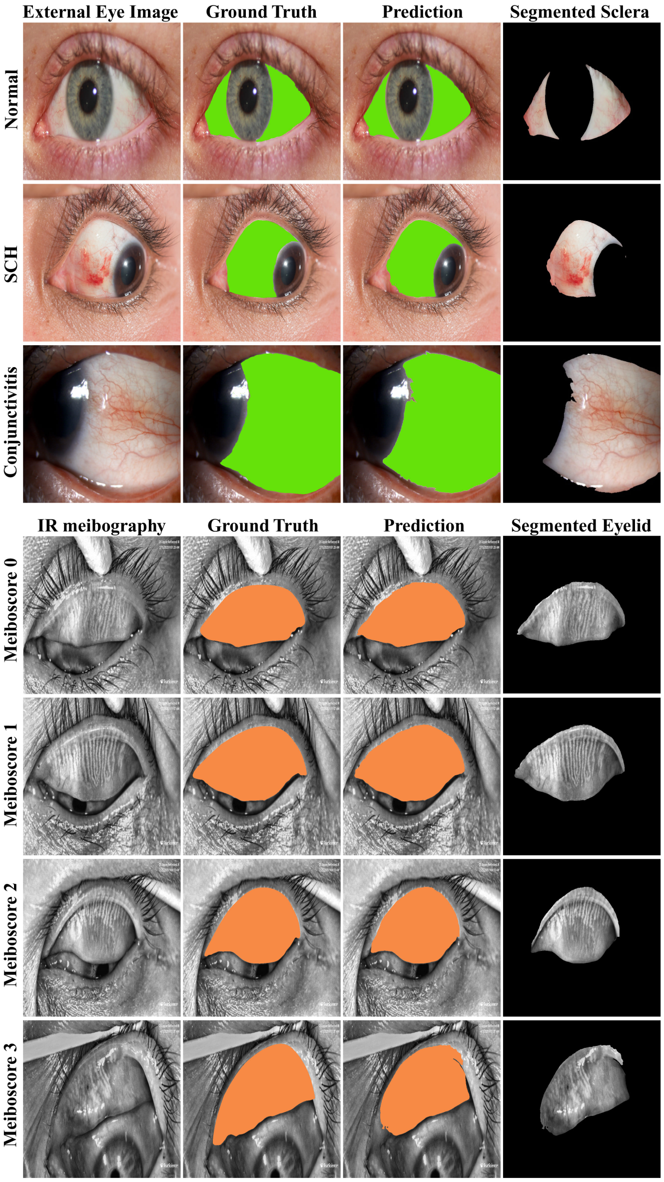

Fig. 4. Predictions utilizing SU-Net for scleral region segmentation in various external eye images, as well as for eyelid area segmentation in meibography images with differing meiboscores. A comparison is made between the ground truth and the predictions, showcasing the predicted regions extracted from the original images.

III. RESULTS

A. Segmentation of Sclera or Eyelid

For enhanced segmentation of MG and SCH, it is essential to eliminate the interference caused by the skin and eyelash areas, as these regions can impede accurate recognition. Therefore, removing these areas is a crucial step in achieving more precise segmentation results. The effectiveness of the SU-Net is assessed using the SBVPI dataset and MGD-1K dataset. The model's performance is evaluated by determining the accuracy, IOU, and F1 score.

For the RGB module, on the SBVPI dataset, SU-Net demonstrated an accuracy of 0.992, an IOU of 0.977, and an F1 score of 0.982. These metrics, combined with the information in Table II, reinforce the superior performance of SU-Net in this specific task. In Fig. 4, representative RGB images of three types are presented alongside their scleral ground truth and scleral segmentations obtained from SU-Net. The scleral area is extracted from the external eye images using a custom algorithm. As can be seen from the figure, SCH and bulbar conjunctivitis made more red bloodshot areas and complex blood vessel patterns appear in the scleral region, without causing obvious interference to the scleral region segmentation. Even for bulbar conjunctivitis photos with incomplete scleral area, SU-Net also shows good segmentation ability. The segmented images successfully remove interference caused by eyelashes and skin, simplifying the following classification process.

TABLE II
SEGMENTATION PERFORMANCE BASED ON THE SBVPI DATASET

Algorithm	Precision	Recall	F1 score
RefineNet-50 [25], [49]	0.960	0.960	0.960
Sclera-Net [50]	0.944	0.982	0.962
SU-Net	**0.993**	**0.971**	**0.982**

For meibography images in the IR module, MGs are only located in the eyelid, while other parts, including the iris, eyelashes, and skin, are unnecessary or even disturbing for subsequent processing. The meibography images of four different dropout severities have their eyelid regions extracted in the same manner as scleral areas. Although the four MG images have different meiboscores, the eyelid segmentation effect is not affected. There is no significant difference between eyelids. The eyelid segmentation achieves an accuracy of 0.990, effectively avoiding interference from skin and eyelashes in the meibography (Fig. 4).

B. Three-class Classification for RGB images

From an image feature perspective, both SCH and bulbar conjunctivitis can cause redness in the eye, leading to significant anxiety for patients. In both cases, the affected eye may appear red or bloodshot due to inflammation or blood accumulation. In SCH, the redness is typically more localized, with a well-defined border and a bright red color due to the presence of fresh blood. Bulbar conjunctivitis usually results in a more diffuse redness across the entire eye, and the color may be less bright.

For the RGB module, in our research, we fine-tuned the YOLOv5 model to categorize three distinct eye conditions: healthy white eyes, eyes affected by bulbar conjunctivitis, and eyes with SCH. A healthy white eye is characterized by a clear, white sclera, whereas eyes with conjunctivitis exhibit inflammation, redness, and frequent discomfort. In contrast, SCH eyes display a prominent buildup of blood on the surface of the sclera.

The assessment results demonstrated the model's effectiveness in differentiating between the various eye conditions, consistently achieving an accuracy of 98.7% with an F1 score of

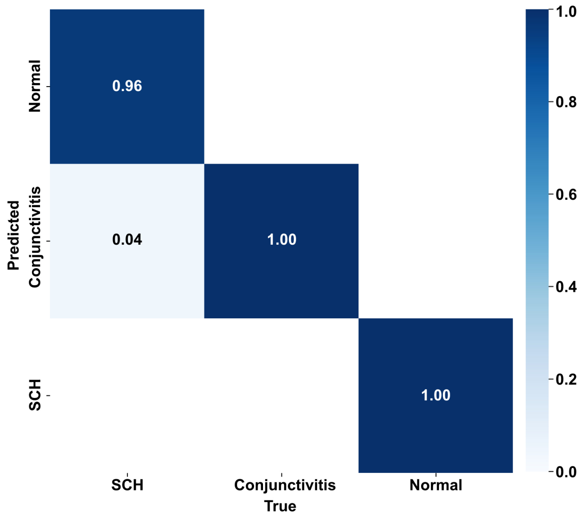

Fig. 5. The performance of the three-class classification is quantitatively assessed using the confusion matrix for SU-Net.

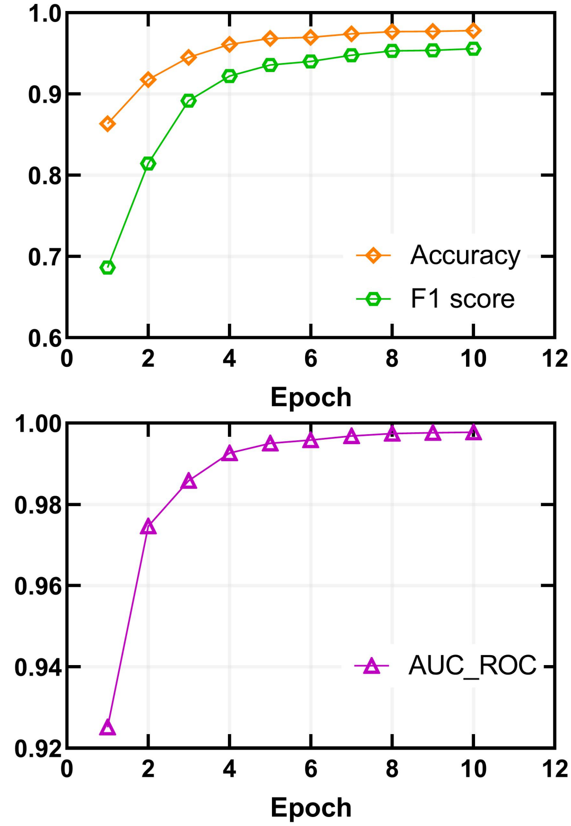

Fig. 6. Progress of performance metrics during the training process for scleral area segmentation task. The evaluated metrics comprise the overall accuracy, F1 score, and AUC-ROC curve.

0.980. External validation with the public Kaggle conjunctivitis dataset added an additional layer of reliability, showcasing the model's effectiveness in different clinical contexts (data not shown). Compared with other methods that simply distinguish eye redness from normal eye images, our method deepens the detail of classification and represents a more accurate eye healthcare. This underlines the possible utility of the YOLOv5 algorithm in automating ocular condition diagnosis, eventually facilitating the early detection and prompt treatment of diverse eye diseases. Fig. 5 demonstrates a confusion matrix that illustrates the distinct allocations of diverse predicted outcomes for different input RGB images corresponding to the three particular states of the scleral region. Accurate classification is crucial for subsequent assessment.

C. Measurement of the SCH Area and Extraction of Vessels with Specified Thickness

Fig. 6 illustrates the training progress of the CNN model. The model's performance (accuracy, F1 score, and AUC-ROC) on the validation subset frames is displayed, attaining an accuracy of 96.2% as shown in Table III. Throughout the training process, there is a consistent improvement in accuracy and F1 scores, further emphasizing the effectiveness of our approach. Additionally, the AUC-ROC metric exhibits an increasing trend for the task, regardless of the differences in their respective patterns. This indicates that the proposed framework is capable of adapting to SCH area segmentation tasks while maintaining high performance and reliability.

The system delivers a quantitative analysis of the intricate hemorrhage region in images identified as SCH, employing self-developed algorithms depicted in Fig. 7. This analysis is compared with manual annotations as the ground truth. Furthermore, for SCH images ranging from mild to severe degrees, the system calculates the percentage of SCH region pixels within the scleral area, which is beneficial for disease monitoring and recovery tracking (Fig. 8). These findings showcase the system's precision in determining SCH severity and providing a more objective assessment of eye redness.

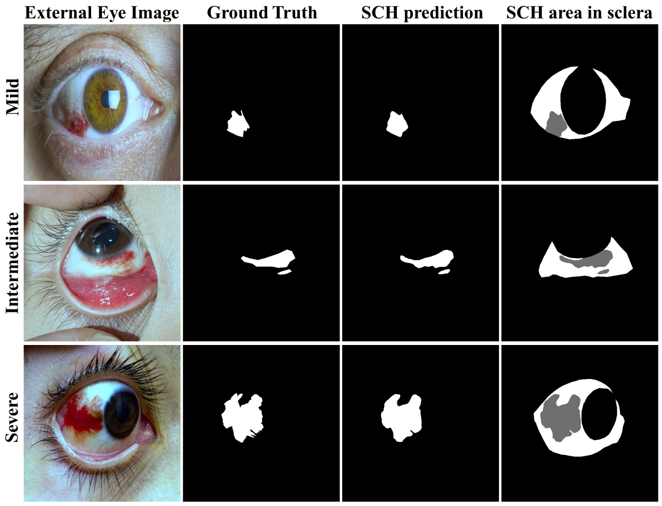

Fig. 7. SCH segmentation and area measurement in the scleral region.

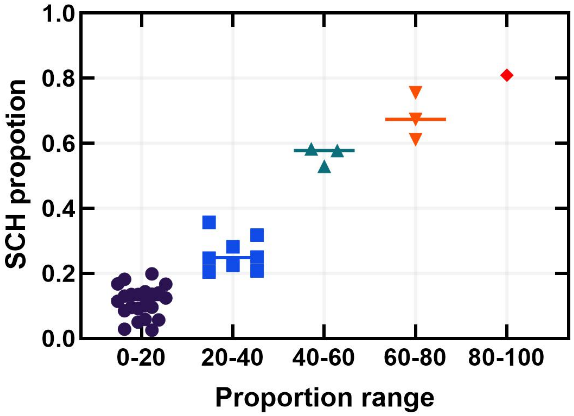

Fig. 8. Patients with varying SCH area proportions and distinct proportion groups. The proportions are segmented into five intervals, with each interval comprising twenty percent.

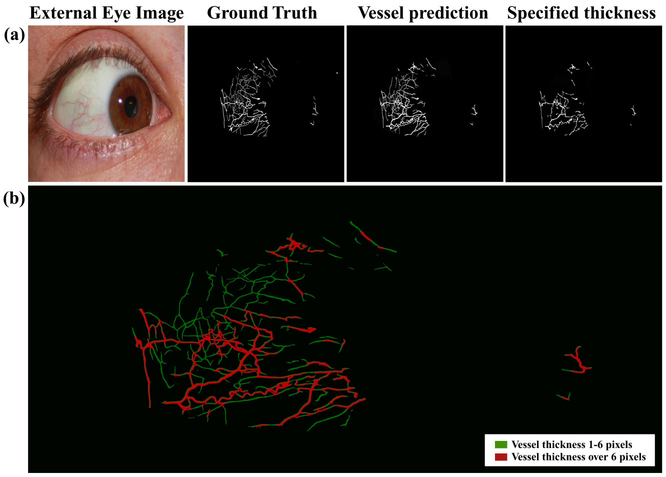

Fig. 9. (a) Prediction of vessel presence and extraction of thickness. (b) Closeup illustrations of the extracted vascular structures.

For images recognized as bulbar conjunctivitis, the system isolates dilated vessels that surpass a certain thickness. While assessing, probability maps are transformed into binary format with a 0.5 threshold prior to determining the accuracy. This measurement can provide a more detailed segmentation of vessels. This isolation enables a more distinct visualization of the most dilated blood vessels, reducing the visual disturbance from smaller vessels (Fig. 9(a)). The vessel extraction process can be effortlessly adapted to accommodate the characteristics of the vessels under examination. As demonstrated in Fig. 9(b), vessels with a thickness exceeding 6 pixels are isolated.

D. *Identification of MG area ratio and MG irregularities*

After the deep learning-based segmentation model is trained with the input images, meibography images could be transformed into images containing the segmented labels of the MG or eyelid. The algorithm attains an overall accuracy score of 93.7% for MG segmentation as demonstrated in Table III. A representative example of the original IR image and images

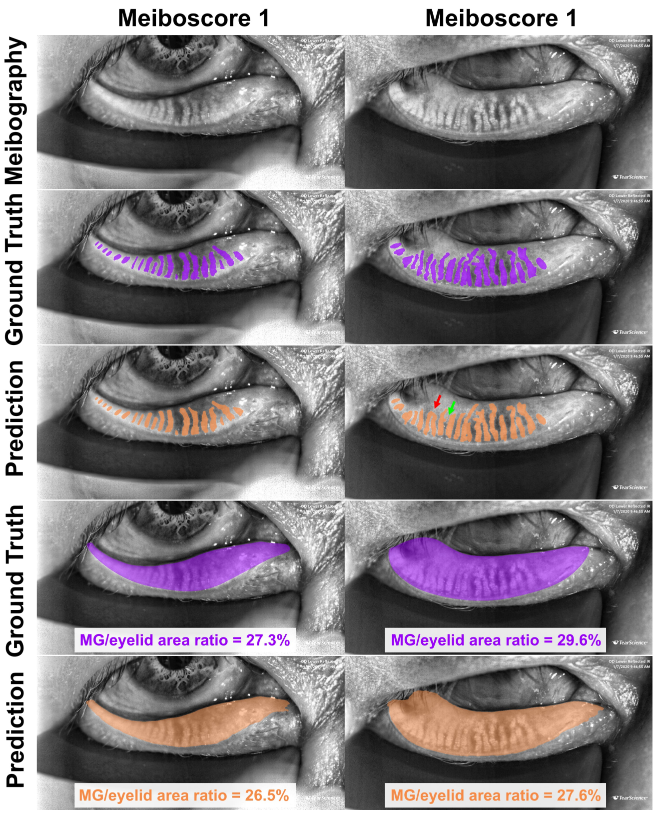

Fig. 10. MG-to-eyelid area ratio calculation and comparison of the same meiboscore. The ground truth masks of MGs and eyelids are illustrated in purple transparent color, and the corresponding prediction masks by the deep learning model are demonstrated in orange transparent color. The red and green arrows indicate the false crossing gland and false recognition gland segmentation respectively.

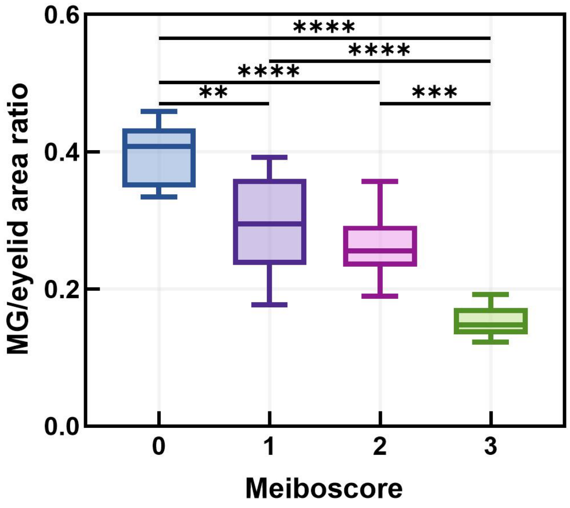

Fig. 11. MG-to-eyelid area ratio across four distinct meiboscore groups, showcasing the significant difference.

TABLE III
PERFORMANCE EVALUATION OF DUAL-MODE IMAGE TASKS

Task	Precision	Recall	F1 score	Specificity (SP)	Accuracy
SCH region identification	0.969	0.943	0.956	0.987	0.962
MG area segmentation	0.898	0.881	0.889	0.960	0.937
MG irregularity identification	0.784	0.778	0.781	0.886	0.881

overlaid by the ground truth annotation and deep learning segmented output for identical meiboscore is shown in Fig. 10. Furthermore, as the meiboscore escalates, the proportion of the MG area relative to the entire analyzed eyelid area diminishes (Fig. 11). The system effectively detects the four types of irregularities (overlapping, shortening, thickening, and tortuosity) with a mean accuracy of 88.1%, and the corresponding confusion matrix is demonstrated in Fig. 12. As illustrated in Fig. 13, meibography images with a higher dropout area, such as Meiboscore 3, exhibit more shortening MGs and a reduced overlapping area compared to meibography images with a lower dropout, such as Meiboscore 0. To our knowledge, this is the first time that various features of MG morphological irregularities have been associated with MGD as an early diagnostic indicator.

From Meiboscore 0 to 3, the overlapping MG ratio experiences a 17% decrease, while the shortening MG ratio sees a 12% increase, as depicted in Fig. 14. Within the dataset, thickening MGs exhibit a slight upward trend as the meiboscore rises. However, tortuosity MGs do not display a discernible pattern. Notably, the morphological parameters undergo significant changes across the four meiboscore groups, indicating the association between meiboscores and MG irregularities.

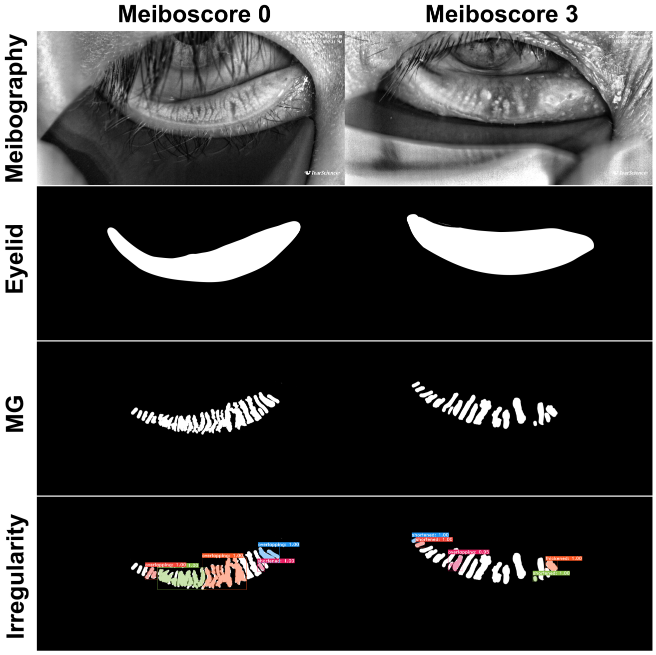

Fig. 13. Identification of MG irregularities within segmented MG regions. Two representative meibography images showcasing varying percentages of MG atrophy.

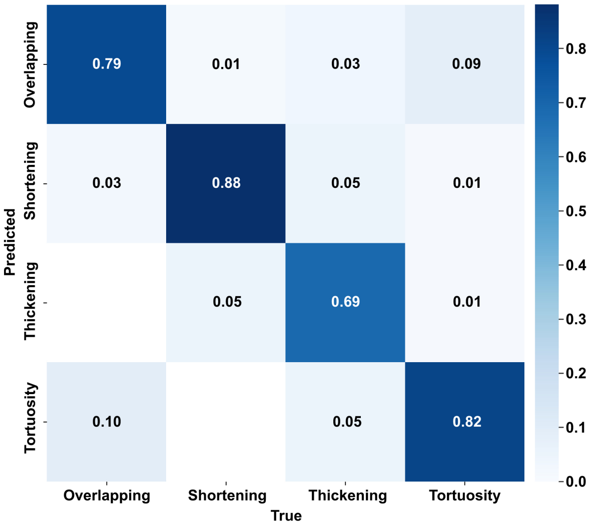

Fig. 12. The performance of the MG irregularity classification is quantitatively assessed using the confusion matrix. Four kinds of MG irregularities are overlapping, shortening, thickening, and tortuosity.

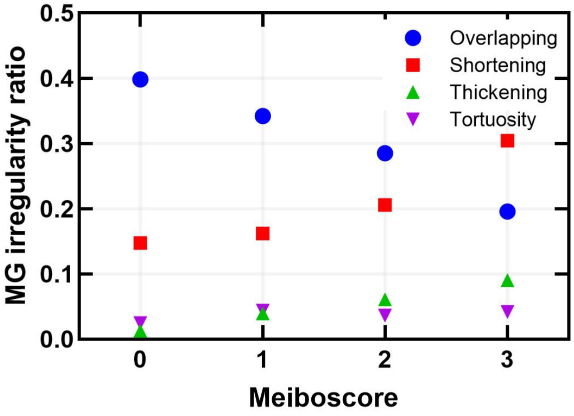

Fig. 14. Variations in irregularly shaped MG types and their corresponding ratio alterations across distinct meiboscore ranges.

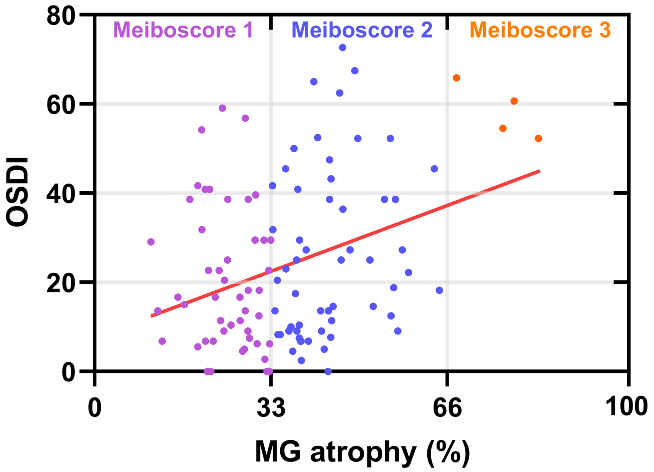

Fig. 15. Ocular Surface Disease Index (OSDI) scores vs. MG atrophy (%). The data points are colored according to different Meiboscores ranging from 1 to 3.

E. Intergration with clinical questionnaires and portable IR camera for home inspection

Simultaneously processing image and text information is a crucial aspect of modern data analysis, as it facilitates a more comprehensive understanding and interpretation of complex datasets. Additional features or markers can be used as references to enhance the accuracy of OSD detection. The OSDI is a standardized, validated questionnaire designed to assess the severity of ocular surface symptoms and their impact on vision-related functioning in patients with dry eye disease and other ocular surface disorders. The OSDI questionnaire consists of 12 questions that cover three domains [51]. Furthermore, a positive correlation exists between the OSDI and MG atrophy across different meiboscore groups. This highlights the importance of the OSDI as an additional metric, underscoring its significance in evaluating the severity of MGD (Fig. 15). Eye redness, pain, and blurred vision are three key metrics for evaluating eye health as shown in Table IV. To enable patients to conduct self-examinations and assist doctors in acquiring more comprehensive information, we have incorporated relevant scales into our system. This integration empowers patients to take a proactive role in their own ocular health management and provides healthcare professionals with valuable data to make well-informed decisions and offer targeted treatments.

Utilizing a USB camera equipped with 850 nm IR LED arrays, the portable device enables the acquisition of high-contrast meibography images, establishing it as a convenient tool for daily self-checks (Fig. 16). The six IR lights are highlighted in the red box in the figure. Housed within a handheld metal container, the system easily attaches to a smartphone, as depicted in Fig. 17. The images captured by this device exhibit high quality and are suitable for evaluating various irregularities. Moreover, the accompanying smartphone app empowers users to customize parameters such as intensity and contrast, enhancing user-friendliness while ensuring optimal image quality. Additionally, the captured images undergo processing to identify irregularities. The joint design of the algorithm and portable IR camera for home inspection presents a novel approach to enhancing the efficiency and accuracy of home inspection. The integrating a portable IR camera in our system allows for greater accessibility and convenience for patients, enabling them to perform meibography inspections at home without the need to visit a clinic or hospital, which can be particularly beneficial for individuals with mobility constraints, limited access to healthcare facilities, or during situations like the COVID-19 pandemic when in-person visits may be restricted. Furthermore, at-home meibography inspections

TABLE IV
EYE HEALTH QUESTIONNAIRE

No.	Screening Questions
I	Have you noticed any redness, swelling, or discharge in your eyes?
II	Are you experiencing any discomfort or pain in your eyes? If so, can you describe the intensity, frequency, and duration of the pain?
III	Have you had any recent eye injuries or accidents that may have affected your vision or eye health?
IV	Have you experienced any changes in your vision, such as blurriness, double vision, or difficulty focusing? If so, can you describe the intensity, frequency, and duration of the pain?

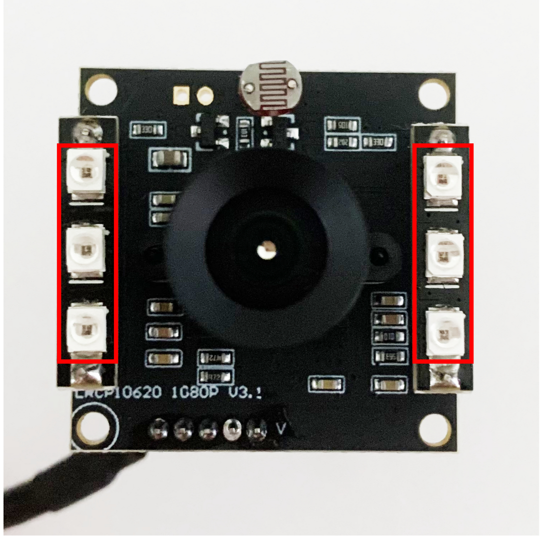

Fig. 16. A USB-enabled imaging sensor featuring an integrated IR LED array of 850 nm (highlighted in red box) designed for a portable meibography device.

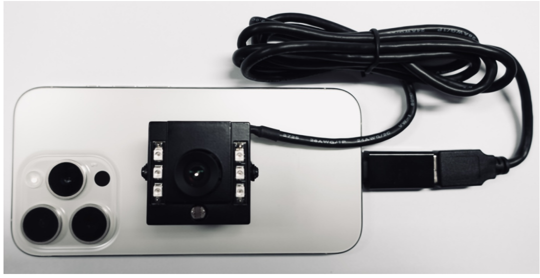

Fig. 17. The encapsulated portable IR meibography prototype device connected to a smartphone.

using a portable IR camera can facilitate the early detection and routine monitoring of MGD. This can help patients and healthcare providers to identify and address potential issues in a timely manner, improving overall prognosis and treatment outcomes.

IV. DISCUSSION

Despite advancements in diagnostics and therapeutics, challenges and limitations persist in managing OSDs. Three main areas of limitation exist in the early detection and continuous monitoring of OSDs: the discrepancy between patient numbers and limited medical resources, inadequate early detection and measurement indicators, and limited home monitoring options. Dry eye disease, conjunctivitis, and SCH are prevalent conditions that strain ophthalmic care systems, resulting in inadequate access to specialized care, long waiting times, and delayed diagnosis and treatment [52]–[54]. This situation underscores the need for automated diagnosis based on limited medical resources. Our proposed system offers a more efficient and accurate method for diagnosing OSDs, facilitating timely and precise treatments. Furthermore, it facilitates patients in remote regions to have equitable access to quality care. By automating the diagnostic process, our system has the potential to significantly reduce healthcare costs through streamlined operations.

The detection and quantification of OSDs have garnered increased attention in recent years. In the domain of ocular redness assessment, Verma et al. developed a CNN-based classifier capable of distinguishing between a healthy and a red human eye, particularly aimed at detecting hyperemia through color extraction from images [55]. However, this preliminary assessment failed to identify a direct link to specific eye diseases. Sirazitdinova et al. trained a random decision forest classifier to assess external eye redness, finding that accurate computation of ocular redness heavily relies on effective sclera segmentation [10]. Further, Curti et al. developed a CNN model for conjunctival segmentation and the quantification of hyperemia scores, achieving an impressive average accuracy of 0.94 and an IOU score of 0.88 [56]. Our research further categorizes subtypes of ocular redness, including SCH and bulbar conjunctivitis, and quantifies the severity accordingly, thereby preventing mismanagement and alleviating patient concerns. For MGD detection, Wang et al. introduced a deep learning algorithm based on the pyramid scene parsing network to digitally segment MG atrophy areas and calculate percent atrophy in meibography images, achieving a 95.4% accuracy and 66.7% IOU in analyzing gland atrophy regions [47]. Despite these advancements, precise segmentation of individual MGs remained unaddressed. Setu et al. employed a U-Net-based method with transfer learning for automatic MG segmentation and precise assessment of individual MG morphology, including parameters such as MG number, length, width, and tortuosity, achieving average precision, recall, and F1 scores of 83%, 81%, and 84%, respectively [41]. Additionally, Saha et al. developed a deep learning model incorporating skip connections and residual connections for quantitative evaluation of MG morphology, successfully eliminating reflection from original MG images without impacting meiboscore grading [26]. Our multi-stage, deep learning-based approach demonstrates enhanced accuracy and generalization capabilities using two datasets, considering the quantification of both individual and collective MG metrics. Moreover, user-friendly and accurate home monitoring devices such as MeiboVue and Ezer Sapphire, are capable of capturing MG images [22]. Deep learning algorithms and models will further empower these portable devices alongside our proposed IR MG camera. By integrating the detection and monitoring of both ocular redness and MGD through dual-mode imaging techniques, we contribute to the development of a comprehensive system.

Diagnosing dry eye syndrome presents a challenge due to the lack of a singular defining symptom or diagnostic criterion [57]. An effective diagnosis necessitates considering both the patient's symptoms and clinical signs [58]. Critical diagnostic features for dry eye include tear break-up time (TBUT), MGD, OSDI, and the Schirmer test score, with TBUT traditionally administered by healthcare professionals in a clinical setting. Furthermore, recent advancements have seen the application of learning-based methods to characterize rates of MG dropout [26], [59]. Research indicates a significant correlation between MG thickness and TBUT, and MG loss has been found to be significantly related to tear film characteristics, including the thickness and stability of the lipid layer [60]. However, the relationship between morphological irregularities in the MGs and MGD necessitates further investigation. MG morphological abnormalities are a prevalent clinical indicator of MGD, yet there is a scarcity of automated methods for providing standardized quantifications of morphological features for individual glands [61], [62]. Meibography imaging plays a crucial role in revealing the morphology of multiple glands, underscoring the importance of both individual gland features and the overall gland morphology. Wang et al. have employed gland segmentations to analyze individual gland characteristics, including local contrast, length, width, and tortuosity, thereby facilitating the quantitative analysis of gland morphological features and the identification of ghost glands [61], [63].

This research work acknowledges certain limitations that are important to address for future development and validation. Firstly, the integration of the portable IR meibography camera is in its initial stages and has not undergone large-scale clinical validation. In collaboration with clinical partners, we have made efforts to refine the prototype, testing it on a small group of subjects ($n > 3$) who provided feedback. While the camera facilitates easy home inspections, there is a recognized need for proper patient training to ensure correct usage. Untrained individuals often find it challenging to fully expose the eyelids, particularly the upper eyelid, during infrared photography of the MGs [64]. Additionally, variability in lighting and room conditions during at-home inspections can potentially impact the quality of the captured images, leading to issues such as underexposure or overexposure. Secondly, our model has shown proficiency in distinguishing between SCH and bulbar conjunctivitis. However, there is considerable scope for expansion. The current limitations could lead to overlooking potential interferences, such as conjunctival congestion, which is characterized by the dilation of blood vessels in the conjunctiva. While conjunctival congestion is a symptom of conjunctivitis, it is not the sole defining feature. Conditions such as corneal endotheliitis, iridocyclitis, and Posner-Schlossman syndrome, which also manifest as conjunctival congestion but are not conjunctivitis, highlight the need for our model to differentiate between these conditions more effectively. Thirdly, our current datasets for IR and RGB images are distinct, having been collected at different times, locations, and from different subjects, resulting in no direct correlation between the two sets. The images from each dataset are trained separately through the segmentation network, with their trained models validated independently.

For future work, first, we are committed to enhancing the widespread adoption of our system through the execution of extensive clinical trials. These trials will assess the system's performance across diverse populations and environments, with the goal of providing valuable insights and pinpointing areas for improvement. In meibography imaging, additional efforts are required to assist untrained individuals. This includes providing video tutorials to ensure consistent imaging results and incorporating silicone everters to aid in effectively exposing the eyelids [65]. Additionally, more image preprocessing algorithms will be incorporated to ensure that the images are well-exposed. Furthermore, telemedicine features will be further integrated to facilitate remote consultations with eye care specialists. Second, we intend to expand our dataset to include conditions such as corneal endotheliitis, iridocyclitis, and Posner-Schlossman syndrome. By refining our deep learning model, we aim to cover a broader spectrum of complex conditions, thereby improving our model's capacity to accurately distinguish between conjunctivitis and other conditions that exhibit similar symptoms, including variable and diffuse distributions of SCH. Moreover, we plan to broaden the detection capabilities of our system by incorporating more OSDs such as pterygium and episcleritis. Finally, in our subsequent research endeavors, we aim to establish a linkage between the IR and RGB datasets. This will involve acquiring dual-mode images of the same patients simultaneously and conducting correlation analyses through the application of image fusion techniques. This approach is anticipated to significantly advance personalized eye care by enabling us to obtain more precise information about the OSD status and conditions of individual patients. Ultimately, these advancements will bolster the diagnostic and monitoring capabilities of our system, offering a more comprehensive and nuanced understanding of ocular health.

V. CONCLUSION

In this study, we present a dual-mode imaging system designed specifically for the early detection and continuous monitoring of OSDs, with a focus on SCH, bulbar conjunctivitis, and MGD. Our approach extends beyond mere detection, encompassing a broader spectrum of OSDs through automatic analysis. Utilizing a multi-stage deep learning model, our system enhances diagnostic accuracy and efficiency for both IR meibography and RGB external eye imagery. Our methodology has demonstrated improved classification accuracy in identifying ocular redness and determining the extent of SCH regions. Furthermore, we have optimized MGD detection by precisely analyzing MG area ratios and identifying structural anomalies.

We are currently refining our system to enable long-term monitoring through the integration of portable IR cameras. This development promises to facilitate at-home inspections, significantly reducing costs and enhancing the accessibility of diagnosing and monitoring various eye conditions. Ultimately, our comprehensive system seeks to transform ocular health management by offering accurate, efficient, and user-friendly solutions for the detection and monitoring of eye disorders.

REFERENCES

[1] I. K. Gipson, "The ocular surface: the challenge to enable and protect vision: the friedenwald lecture," *Investigative Ophthalmology & Visual Science*, vol. 48, no. 10, pp. 4391–4398, 2007.

[2] E. K. Akpek, G. Amescua, M. Farid, F. J. Garcia-Ferrer, A. Lin, M. K. Rhee, D. M. Varu, D. C. Musch, S. P. Dunn, and F. S. Mah, "Dry eye syndrome preferred practice pattern®," *Ophthalmology*, vol. 126, no. 1, pp. P286–P334, 2019.

[3] H. Pult and J. S. Wolffsohn, "The development and evaluation of the new ocular surface disease index-6," *The Ocular Surface*, vol. 17, no. 4, pp. 817–821, 2019.

[4] D. R. Pur, S. H. Krance, A. Pucchio, R. N. Miranda, and T. Felfeli, "Current uses of artificial intelligence in the analysis of biofluid markers involved in corneal and ocular surface diseases: a systematic review," *Eye*, vol. 37, no. 10, pp. 2007–2019, 2023.

[5] R. Chen, W. Zeng, W. Fan, F. Lai, Y. Chen, X. Lin, L. Tang, W. Ouyang, Z. Liu, and X. Luo, "Automatic recognition of ocular surface diseases on smartphone images using densely connected convolutional networks," in *2021 43rd Annual International Conference of the IEEE Engineering in Medicine & Biology Society (EMBC)*. IEEE, 2021, pp. 2786–2789.

[6] C. E. Starr, P. K. Gupta, M. Farid, K. A. Beckman, C. C. Chan, E. Yeu, J. A. Gomes, B. D. Ayers, J. P. Berdahl, E. J. Holland, *et al.*, "An algorithm for the preoperative diagnosis and treatment of ocular surface disorders," *Journal of Cataract & Refractive Surgery*, vol. 45, no. 5, pp. 669–684, 2019.

[7] D. S. W. Ting, L. R. Pasquale, L. Peng, J. P. Campbell, A. Y. Lee, R. Raman, G. S. W. Tan, L. Schmetterer, P. A. Keane, and T. Y. Wong, "Artificial intelligence and deep learning in ophthalmology," *British Journal of Ophthalmology*, 2018.

[8] Z. Zhang, Y. Wang, H. Zhang, A. Samusak, H. Rao, C. Xiao, M. Abula, Q. Cao, and Q. Dai, "Artificial intelligence-assisted diagnosis of ocular surface diseases," *Frontiers in Cell and Developmental Biology*, vol. 11, p. 1133680, 2023.

[9] Y. Li, P. W. Chiu, Y. Zhu, Y. Cao, V. Tam, A. Lee, and E. Y. Lam, "Monitoring the progress of subconjunctival hemorrhage through spectral reconstruction from rgb images," in *Computational Optical Imaging and Artificial Intelligence in Biomedical Sciences*, vol. 12857. Proceedings of the SPIE, 2024, pp. 72–76.

[10] E. Sirazitdinova, M. Gijs, C. J. Bertens, T. T. Berendschot, R. M. Nuijts, and T. M. Deserno, "Validation of computerized quantification of ocular redness," *Translational Vision Science & Technology*, vol. 8, no. 6, pp. 31–31, 2019.

[11] C. Chase, A. Elsawy, T. Eleiwa, E. Ozcan, M. Tolba, and M. Abou Shousha, "Comparison of autonomous as-oct deep learning algorithm and clinical dry eye tests in diagnosis of dry eye disease," *Clinical Ophthalmology*, pp. 4281–4289, 2021.

[12] H. Abdelmotaal, R. Hazarbasanov, S. Taneri, A. Al-Timemy, A. Lavric, H. Takahashi, and S. Yousefi, "Detecting dry eye from ocular surface videos based on deep learning," *The Ocular Surface*, vol. 28, pp. 90–98, 2023.

[13] E. Vaghefi, S. Hill, H. M. Kersten, D. Squirrell, *et al.*, "Multimodal retinal image analysis via deep learning for the diagnosis of intermediate dry age-related macular degeneration: a feasibility study," *Journal of Ophthalmology*, vol. 2020, 2020.

[14] S. Bonini, "The red eye," *European Journal of Ophthalmology*, vol. 31, no. 6, pp. 2843–2849, 2021.

[15] M. A. Lemp, L. A. Crews, A. J. Bron, G. N. Foulks, and B. D. Sullivan, "Distribution of aqueous-deficient and evaporative dry eye in a clinic-based patient cohort: a retrospective study," *Cornea*, vol. 31, no. 5, pp. 472–478, 2012.

[16] E. Daniel, M. G. Maguire, M. Pistilli, V. Y. Bunya, G. M. Massaro-Giordano, E. Smith, P. A. Kadakia, P. A. Asbell, *et al.*, "Grading and baseline characteristics of meibomian glands in meibography images and their clinical associations in the dry eye assessment and management (dream) study," *The Ocular Surface*, vol. 17, no. 3, pp. 491–501, 2019.

[17] G. Giannaccare, L. Vigo, M. Pellegrini, S. Sebastiani, and F. Carones, "Ocular surface workup with automated noninvasive measurements for the diagnosis of meibomian gland dysfunction," *Cornea*, vol. 37, no. 6, pp. 740–745, 2018.

[18] Z. Zhang, X. Lin, X. Yu, Y. Fu, X. Chen, W. Yang, and Q. Dai, "Meibomian gland density: An effective evaluation index of meibomian gland dysfunction based on deep learning and transfer learning," *Journal of Clinical Medicine*, vol. 11, no. 9, p. 2396, 2022.

[19] E. Y.-C. Kang, L. Yeung, Y.-L. Lee, C.-H. Wu, S.-Y. Peng, Y.-P. Chen, Q.-Z. Gao, C. Lin, C.-F. Kuo, and C.-C. Lai, "A multimodal imaging–based deep learning model for detecting treatment-requiring retinal vascular diseases: model development and validation study," *JMIR Medical Informatics*, vol. 9, no. 5, p. e28868, 2021.

[20] M. Uchino, N. Yokoi, M. Kawashima, Y. Ryutaro, Y. Uchino, and K. Tsubota, "Treatment trends in dry eye disease and factors associated with ophthalmic follow-up discontinuation in japan," *Journal of Clinical Medicine*, vol. 8, no. 8, p. 1120, 2019.

[21] Y. Li, H. S. Kan, Y. Zhu, Y. Cao, V. Tam, A. Lee, and E. Y. Lam, "An intelligent and handheld device for early identification of meibomian gland irregularities," in *Ophthalmic Technologies XXXIV*, vol. 12824. Proceedings of the SPIE, 2024, pp. 77–81.

[22] H. Retana, E. Bojorges, and E. Quintela, "Development of alpha prototype of handheld device for meibography," in *Congreso Nacional de Ingeniería Biomédica*. Springer, 2022, pp. 448–458.

[23] Y. Li, P. W. Chiu, Y. Zhu, V. Tam, A. Lee, and E. Y. Lam, "A deep-learning-enabled monitoring system for ocular redness assessment," in *2023 IEEE Biomedical Circuits and Systems Conference (BioCAS)*. IEEE, 2023, pp. 1–5.

[24] P. Rot, M. Vitek, K. Grm, Ž. Emeršič, P. Peer, and V. Štruc, "Deep sclera segmentation and recognition," *Handbook of Vascular Biometrics*, pp. 395–432, 2020.

[25] M. Vitek, P. Rot, V. Štruc, and P. Peer, "A comprehensive investigation into sclera biometrics: a novel dataset and performance study," *Neural Computing and Applications*, vol. 32, pp. 17 941–17 955, 2020.

[26] R. K. Saha, A. M. Chowdhury, K.-S. Na, G. D. Hwang, Y. Eom, J. Kim, H.-G. Jeon, H. S. Hwang, and E. Chung, "Automated quantification of meibomian gland dropout in infrared meibography using deep learning," *The Ocular Surface*, vol. 26, pp. 283–294, 2022.

[27] J. Schindelin, I. Arganda-Carreras, E. Frise, V. Kaynig, M. Longair, T. Pietzsch, S. Preibisch, C. Rueden, S. Saalfeld, B. Schmid, *et al.*, "Fiji: an open-source platform for biological-image analysis," *Nature Methods*, vol. 9, no. 7, pp. 676–682, 2012.

[28] R. Dorothy, R. Joany, R. J. Rathish, S. S. Prabha, S. Rajendran, and S. Joseph, "Image enhancement by histogram equalization," *International Journal of Nano Corrosion Science and Engineering*, vol. 2, no. 4, pp. 21–30, 2015.

[29] E. Y. Lam, "Combining gray world and retinex theory for automatic white balance in digital photography," in *Proceedings of the Ninth International Symposium on Consumer Electronics, 2005.(ISCE 2005)*. IEEE, 2005, pp. 134–139.

[30] O. Ronneberger, P. Fischer, and T. Brox, "U-net: Convolutional networks for biomedical image segmentation," in *Medical Image Computing and Computer-Assisted Intervention–MICCAI 2015: 18th International Conference, Munich, Germany, October 5-9, 2015, Proceedings, Part III 18*. Springer, 2015, pp. 234–241.

[31] G. Jocher, A. Chaurasia, A. Stoken, J. Borovec, Y. Kwon, K. Michael, J. Fang, C. Wong, Z. Yifu, D. Montes, *et al.*, "ultralytics/yolov5: v6. 2-yolov5 classification models, apple m1, reproducibility, clearml and deci. ai integrations," *Zenodo*, 2022.

[32] Z. Ji, Y. Wu, X. Zeng, Y. An, L. Zhao, Z. Wang, and I. Ganchev, "Lung nodule detection in medical images based on improved yolov5s," *IEEE Access*, 2023.

[33] M. Elshahawy, A. Elnemr, M. Oproescu, A.-G. Schiopu, A. Elgarayhi, M. M. Elmogy, and M. Sallah, "Early melanoma detection based on a hybrid yolov5 and resnet technique," *Diagnostics*, vol. 13, no. 17, p. 2804, 2023.

[34] R. Qu, Y. Yang, and Y. Wang, "Covid-19 detection using ct image based on yolov5 network," in *2021 3rd International Academic Exchange Conference on Science and Technology Innovation (IAECST)*. IEEE, 2021, pp. 622–625.

[35] K. Wang, J. H. Liew, Y. Zou, D. Zhou, and J. Feng, "Panet: Few-shot image semantic segmentation with prototype alignment," in *Proceedings of the IEEE/CVF international conference on computer vision*, 2019, pp. 9197–9206.

[36] J. Chen, Y. Lu, Q. Yu, X. Luo, E. Adeli, Y. Wang, L. Lu, A. L. Yuille, and Y. Zhou, "Transunet: Transformers make strong encoders for medical image segmentation," *arXiv preprint arXiv*, vol. 2102, no. 04306, 2021.

[37] R. A. Zeineldin, A. Pollok, T. Mangliers, M. E. Karar, F. Mathis-Ullrich, and O. Burgert, "Deep automatic segmentation of brain tumours in interventional ultrasound data," *Current Directions in Biomedical Engineering*, vol. 8, no. 1, pp. 133–137, 2022.

[38] X. Yan, H. Tang, S. Sun, H. Ma, D. Kong, and X. Xie, "After-unet: Axial fusion transformer unet for medical image segmentation," in *Proceedings of the IEEE/CVF winter conference on applications of computer vision*, 2022, pp. 3971–3981.

[39] D. Hendrycks and K. Gimpel, "Gaussian error linear units (gelus)," *arXiv preprint arXiv:1606.08415*, 2016.

[40] S. Narkhede, "Understanding auc-roc curve," *Towards Data Science*, vol. 26, no. 1, pp. 220–227, 2018.

[41] M. A. K. Setu, J. Horstmann, S. Schmidt, M. E. Stern, and P. Steven, "Deep learning-based automatic meibomian gland segmentation and morphology assessment in infrared meibography," *Scientific Reports*, vol. 11, no. 1, p. 7649, 2021.

[42] A. De Silva, M. V. Perera, N. Wijethilake, S. Jayasinghe, N. D. Nanayakkara, and A. De Silva, "A thickness sensitive vessel extraction framework for retinal and conjunctival vascular tortuosity analysis," *arXiv preprint arXiv:2101.00435*, 2021.

[43] W. Dong, H. Zhou, and D. Xu, "A new sclera segmentation and vessels extraction method for sclera recognition," in *2018 10th International Conference on Communication Software and Networks (ICCSN)*. IEEE, 2018, pp. 552–556.

[44] A. F. Frangi, W. J. Niessen, K. L. Vincken, and M. A. Viergever, "Multiscale vessel enhancement filtering," in *Medical Image Computing and Computer-Assisted Intervention—MICCAI'98: First International Conference Cambridge, MA, USA, October 11–13, 1998 Proceedings 1*. Springer, 1998, pp. 130–137.

[45] K. Drechsler and C. O. Laura, "Comparison of vesselness functions for multiscale analysis of the liver vasculature," in *Proceedings of the 10th IEEE International Conference on Information Technology and Applications in Biomedicine*. IEEE, 2010, pp. 1–5.

[46] S. C. Pflugfelder, S. C. Tseng, O. Sanabria, H. Kell, C. G. Garcia, C. Felix, W. Feuer, and B. L. Reis, "Evaluation of subjective assessments and objective diagnostic tests for diagnosing tear-film disorders known to cause ocular irritation," *Cornea*, vol. 17, no. 1, p. 38, 1998.

[47] J. Wang, T. N. Yeh, R. Chakraborty, X. Y. Stella, and M. C. Lin, "A deep learning approach for meibomian gland atrophy evaluation in meibography images," *Translational Vision Science & Technology*, vol. 8, no. 6, pp. 37–37, 2019.

[48] D. N. Wang, Y. Patel, and M. Luong, "Portable meibography technology using a smartphone device," *Canadian Journal of Ophthalmology*, vol. 55, no. 6, pp. e211–e213, 2020.

[49] G. Lin, A. Milan, C. Shen, and I. Reid, "Refinenet: Multi-path refinement networks for high-resolution semantic segmentation," in *Proceedings of the IEEE conference on computer vision and pattern recognition*, 2017, pp. 1925–1934.

[50] R. A. Naqvi and W.-K. Loh, "Sclera-net: Accurate sclera segmentation in various sensor images based on residual encoder and decoder network," *IEEE Access*, vol. 7, pp. 98 208–98 227, 2019.

[51] R. M. Schiffman, M. D. Christianson, G. Jacobsen, J. D. Hirsch, and B. L. Reis, "Reliability and validity of the ocular surface disease index," *Archives of Ophthalmology*, vol. 118, no. 5, pp. 615–621, 2000.

[52] Y. Y. S. Li, V. Vardhanabhuti, E. Tsougenis, W. C. Lam, and K. C. Shih, "A proposed framework for machine learning-aided triage in public specialty ophthalmology clinics in hong kong," *Ophthalmology and Therapy*, vol. 10, pp. 703–713, 2021.

[53] B. L. Udeh, J. E. Schneider, and R. L. Ohsfeldt, "Cost effectiveness of a point-of-care test for adenoviral conjunctivitis," *The American journal of the medical sciences*, vol. 336, no. 3, pp. 254–264, 2008.

[54] B. Tarlan and H. Kiratli, "Subconjunctival hemorrhage: risk factors and potential indicators," *Clinical Ophthalmology*, pp. 1163–1170, 2013.

[55] S. Verma, L. Singh, and M. Chaudhry, "Classifying red and healthy eyes using deep learning," *International Journal of Advanced Computer Science and Applications*, vol. 10, no. 7, 2019.

[56] N. Curti, E. Giampieri, F. Guaraldi, F. Bernabei, L. Cercenelli, G. Castellani, P. Versura, and E. Marcelli, "A fully automated pipeline for a robust

conjunctival hyperemia estimation," *Applied Sciences*, vol. 11, no. 7, p. 2978, 2021.

[57] S. Kim, D. Park, Y. Shin, M. K. Kim, H. S. Jeon, Y.-G. Kim, and C. H. Yoon, "Deep learning-based fully automated grading system for dry eye disease severity," *Plos One*, vol. 19, no. 3, p. e0299776, 2024.

[58] M. Yazdani, X. Chen, B. Tashbayev, Ø. A. Utheim, S. Ræder, Y. Hua, J. R. Eidet, A. Stojanovic, D. A. Dartt, and T. P. Utheim, "Evaluation of the ocular surface disease index questionnaire as a discriminative test for clinical findings in dry eye disease patients," *Current Eye Research*, vol. 44, no. 9, pp. 941–947, 2019.

[59] Y. Ji, S. Liu, X. Hong, Y. Lu, X. Wu, K. Li, K. Li, and Y. Liu, "Advances in artificial intelligence applications for ocular surface diseases diagnosis," *Frontiers in Cell and Developmental Biology*, vol. 10, p. 1107689, 2022.

[60] H. Pult, B. H. Riede-Pult, and J. J. Nichols, "Relation between upper and lower lids' meibomian gland morphology, tear film, and dry eye," *Optometry and Vision Science*, vol. 89, no. 3, pp. E310–E315, 2012.

[61] J. Wang, S. Li, T. N. Yeh, R. Chakraborty, A. D. Graham, X. Y. Stella, and M. C. Lin, "Quantifying meibomian gland morphology using artificial intelligence," *Optometry and Vision Science*, vol. 98, no. 9, pp. 1094–1103, 2021.

[62] Q. Dai, X. Liu, X. Lin, Y. Fu, C. Chen, X. Yu, Z. Zhang, T. Li, M. Liu, W. Yang, *et al.*, "A novel meibomian gland morphology analytic system based on a convolutional neural network," *IEEE Access*, vol. 9, pp. 23 083–23 094, 2021.

[63] J. Wang, S. Li, T. N. Yeh, R. Chakraborty, S. Yu, and M. C. Lin, "Meibomian gland morphology and ghost prediction with deep learning," *Investigative Ophthalmology & Visual Science*, vol. 61, no. 7, pp. 2634–2634, 2020.

[64] K. Swiderska, M. L. Read, C. A. Blackie, C. Maldonado-Codina, and P. B. Morgan, "Latest developments in meibography: a review," *The Ocular Surface*, vol. 25, pp. 119–128, 2022.

[65] J. S. Wolffsohn, M. Tahhan, M. Vidal-Rohr, O. A. Hunt, and G. Bhogal-Bhamra, "Best technique for upper lid eversion," *Contact Lens and Anterior Eye*, vol. 42, no. 6, pp. 666–669, 2019.